Nanoporous anodic alumina with ohmic contact between substrate and infill: Application to perovskite solar cells

María P Montero-rama, Aurelien Viterisi, Josep Ferré-borrull, Lluis F Marsal

Received: 29 August 2021 | Revised: 10 October 2021 | Accepted: 12 October 2021

DOI: 10.1002/ese3.1002

Energy Science & Engineering Open Access

ORIGINAL ARTICLE

Nanoporous anodic alumina with ohmic contact between substrate and infill: Application to perovskite solar cells

María P. Montero-Rama[1] | **Aurelien Viterisi**[2] | **Josep Ferré-Borrull**[1] | **Lluis F. Marsal**[1]

[1]Departament d'Enginyeria Electrònica Elèctrica i Automàtica, Universitat Rovira i Virgili, Tarragona, Spain

[2]The Institute of Analytical Sciences and Physico-Chemistry for Environment and Materials (IPREM), Technopole Hélioparc, PAU CEDEX 09, France

Correspondence
A. Viterisi, The Institute of Analytical Sciences and Physico-Chemistry for Environment and Materials (IPREM), Technopole Hélioparc, 2 avenue du Président Pierre Angot, 64053 PAU CEDEX 09, France.
Email: aurelien.viterisi@univ-pau.fr
Lluis F. Marsal, Departament d'Enginyeria Electrònica Elèctrica i Automàtica, Universitat Rovira i Virgili, Avinguda Països Catalans 26, 43007 Tarragona, Spain.
Email: lluis.marsal@urv.cat

Funding information
Spanish Ministerio de Ciencia, Innovación y Universidades, Grant/Award Number: RTI2018-094040-B-I00; Agency for Management of University and Research Grants (AGAUR), Grant/Award Number: 2017-SGR-1527

Abstract

The use of a nanostructured aluminum substrate as the cathode for a perovskite photovoltaic device is described. This cathode consists of an aluminum substrate onto which a highly ordered array of aluminum oxide tubular pores was grown *via* anodization. The 1-μm thick pores – arranged in a closed-packed hexagonal pattern – were subsequently selectively etched at the bottom to remove the so-called aluminum oxide barrier layer. The subsequent infiltration of the pores with the components of a methylammonium lead iodide perovskite solar cells, and the completion with a semi-transparent anode, have shown to allow the establishment of an ohmic contact between the substrate itself and the components infiltrated into the Al_2O_3 pores. Indeed, a clear rectifying behavior was observed on the full devices, as well as modest photovoltaic conversion efficiencies. This paper demonstrates that an ohmic contact can be established between the aluminum substrate from which nanoporous anodic alumina was grown, and that the pores can be used to compartmentalize the infill material down to the nanoscopic level.

KEYWORDS

methylammonium-lead iodide, nanoporous anodic alumina, perovskite solar cells, photovoltaics

1 | INTRODUCTION

Nanoporous anodic alumina (NAA) has attracted a great deal of interest in the last two decades. Since the discovery of the two-step anodization procedure by Masuda et al. allowing the fabrication of highly ordered pores at the nanoscopic scale,[1-3] NAA has found applications in various fields of research.[4,5] Indeed, the ability to fabricate layers or laminas with pores having a wide range of thicknesses, diameters, and interpore distances allows them to easily adapt to new applications.[6-9] To date, NAA has been applied to an extremely vast field of research, such as optical sensors,[10-13] biosensors,[12-16] cell culture,[17] drug delivery,[18-20] crystallization enclosures,[21] energy storage, and

energy generation[22-28] devices among others. However, NAA still suffers from the presence of an insulating barrier layer oxide at the bottom of the pores, which does not allow for the establishment of an ohmic contact between the material infiltrated in the pores and the substrate. Consequently, NAA has had limited applications for energy storage devices (batteries, supercapacitors) or energy generation devices (photovoltaic cells), electrical sensors, where the materials infiltrated in the NAA layer would need to be electrically connected to the aluminum electrode. Some research groups have described procedures based on successive reanodization and chemical etching steps, that partly address these setbacks.[29-34] However, these procedures are usually tedious and rarely lead to the complete removal of the barrier layer. They include reanodization steps in sulfuric or oxalic acid using incremental voltage stepdown,[34] incremental current stepdown,[29,34] or constant current successive reanodization[30] and cathodic polarization[31,33] procedures. We have recently reported a procedure to selectively remove the barrier layer on mild anodization NAA with interpore distances superior to 300 nm.[35] That method allows for the complete removal of the barrier layer, allowing, in turn, the establishment of an ohmic contact between the material the pores are filled with and the aluminum substrate.

In order to assess the applicability of the aforementioned method to the manufacture of devices in which an ohmic contact is required, herein, we describe a perovskite solar cell (PSC) in which the nanostructured alumina is used as an enclosure for the perovskite absorber layer (methylammonium lead iodide, $MAPbI_3$) and where the aluminum substrate functions as the cathode. The confinement of the material in the pores is expected to have a significant impact on the crystallization behavior of the $MAPbI_3$, as previously demonstrated.[28,36-39] Additionally, PSC devices in which the absorber perovskite was partly infiltrated in a nanoporous scaffold were shown to have higher stability with respect to standard architectures, since the encapsulation of the perovskite absorber has been shown to retard the diffusion of moisture through the active layer.[28,38,40,41] Moreover, the crystallization of organic materials from nanoscopic enclosures has been demonstrated to follow alternative thermodynamic and kinetic pathways than those from open-air crystallization methods. As such, crystallizations performed in NAA pores often allow the formation of otherwise unstable polymorphs. They can favor the crystallization toward a preferential direction of the lattice and can alter the kinetics of the crystallization process.[42-46]

A barrier layer-free 1-μm thick NAA layer was fabricated as described in our previous report,[35] and the constituent of the perovskite device where successively infiltrated in the pores. The completed device comprised a semi-transparent anode consisting of alternating thin layers of Ag and WO_3,[47] deposited *via* thermal evaporation on top of the hole transport material (HTM). The electrical and photovoltaic properties of the device demonstrated that an ohmic contact was established between the aluminum substrate and the materials infiltrated into the pores. It additionally demonstrated the compatibility of the NAA with the manufacture of complex electrical devices, as the study expounded herein showed a clear rectification behavior and a somehow modest photovoltaic conversion.

2 | RESULTS AND DISCUSSION

The fabrication of the barrier layer-free NAA (f-NAA) substrates was based on a recently published work by our group[35] in which the initial array of ordered pores was submitted to consecutive reanodization and etching steps (see Supporting Information). The pores were subsequently filled with the standard materials used in methylammonium lead iodide perovskite solar cells ($MAPbI_3$) to demonstrate its applicability to photovoltaic devices fabrication.[48-54] The procedure followed to fabricate such a device is depicted in Figure 1B and relies on wet deposition techniques and on the thermal evaporation of a WO_3/Ag semi-transparent anode.[47] A picture depicting a real device is as well shown in Figure 1C. The band diagram of the complete device is depicted in Figure 1A, and shows, as expected, a nearly perfect band alignment of the conduction and valence bands of the absorber with the electron- and hole transport materials (ETM and HTM). Moreover, the work function of the aluminum (from the substrate) and the WO_3 from the anode are, according to literature values, compatible with efficient electron and hole injection.

The choice of the pore size and NAA layer thickness was made in accordance with the PSC architecture prerequisites, *that is*, optimum $MAPbI_3$ domain size, optimum active layer thickness, as well as the minimum thickness practically attainable for NAA layers.[50,55,56] Indeed, the optimum domain size of $MAPbI_3$ PSC devices is in the range of 200-500 nm; therefore, an alumina layer with pore width in the 350-400 nm appeared optimum to us, as it could accommodate a single (crystalline) domain in each pore. Since the optimum active layer thickness is in the 300-500 nm range, and the optimum thickness of the top HTM layer is around 100 and 200 nm, an NAA thickness of 500-600 nm should, therefore, be sufficient to accommodate all afore-mentioned layers and confer added protection toward the decomposition of the $MAPbI_3$ due to the encapsulation effect of the NAA pores. However, we turned our focus to NAA layers with slightly higher

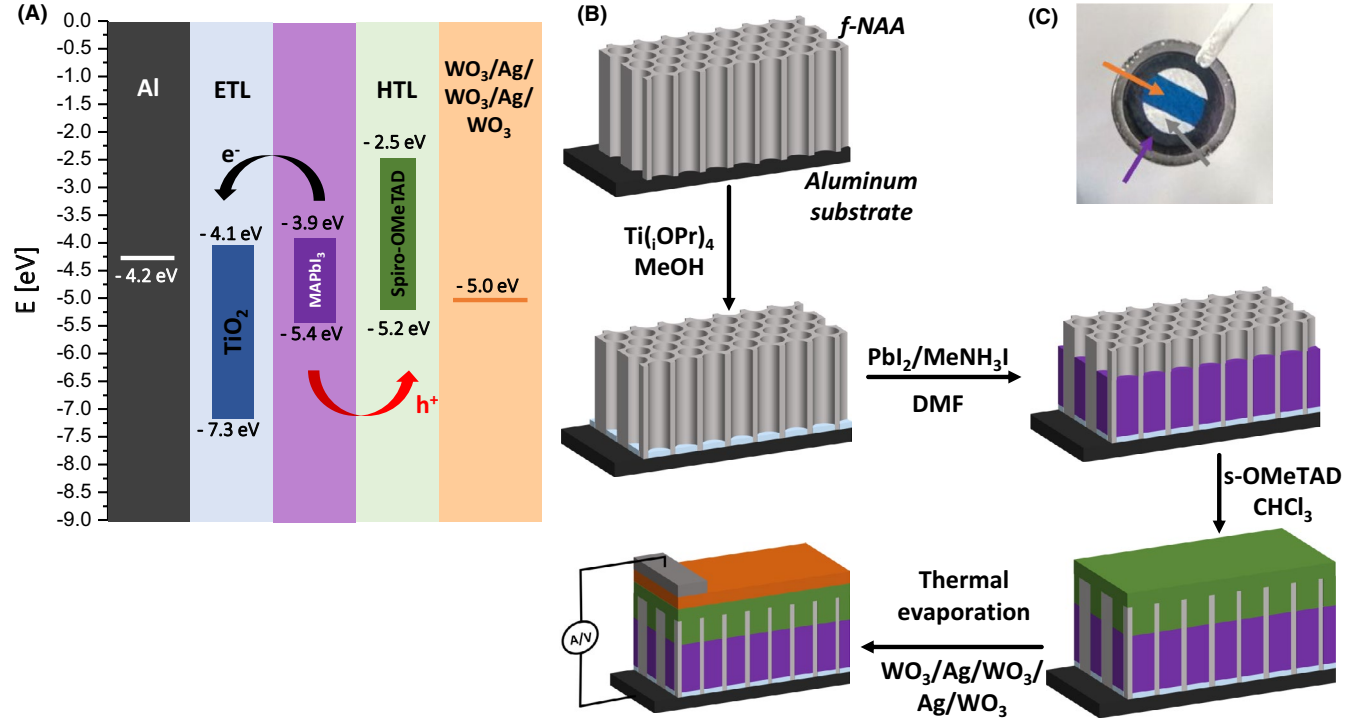

FIGURE 1 A, Band diagram of the NAA-PSC device fabricated in this study; (B) schematic depiction of the solar cell device fabrication; (C) picture of an actual device, the purple arrow points to the $MAPbI_3$ layer, the orange arrow points to the semitransparent anode, while the gray arrow points to the silver upper contact

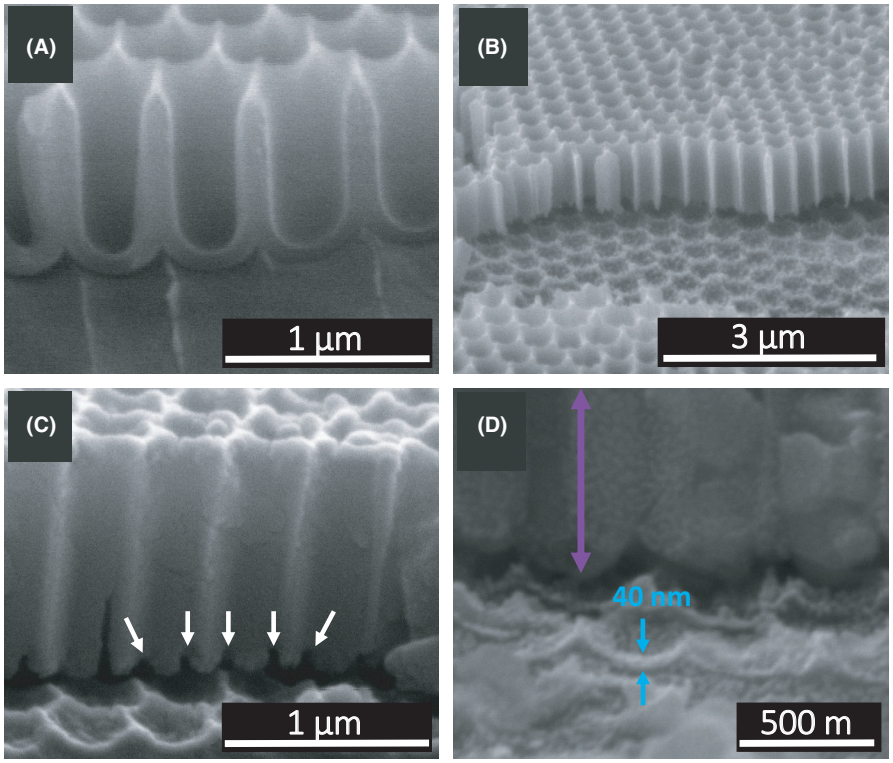

FIGURE 2 A, SEM image of NAA layer prior to the selective removal of the barrier layer. B, SEM image of NAA layer with the barrier layer removed, prior to the TiO_2 infiltration. The layer was intentionally ruptured to reveal the hollow nature of the pore. C, Cross-section SEM image of the barrier layer-free NAA showing the longitudinal openings at the bottom of the pores (white arrows). D, Cross-section SEM image of complete NAA-PSC device showing the bottom of the pores, and the substrate surface covered with a thin layer of TiO_2 approximately 40 nm thick (blue arrows depict the TiO_2 layer, purple arrows depict the $MAPbI_3$ layer). The scales are indicated in each picture

thicknesses (approximately 1000 nm) since NAA layers with aspect ratio over 2 are usually easier to manufacture and characterize, even though NAA substrates with a thickness of 600 nm are in principle achievable. We believe that the optimization of the NAA thickness lies beyond the scope of this study.

The fabrication of the barrier layer-free NAA (f-NAA) substrates consisted of the sequential anodization of aluminum substrates at a constant voltage, chemical etching, and reanodization under a constant current. The initial array of ordered nanopores was grown using the Masuda two-step method at a constant voltage of 195 V, in a 1% phosphoric acid solution at −5ºC, producing NAA with an interpore distance of 350-400 nm. The substrates were subsequently submitted to a partial chemical etching in a 5% phosphoric acid solution at 35°C (see Supporting information for details). This last step, as well as etching the pores' walls, etches the barrier layer to a final thickness of about 80 nm (Figure S1B). NAA was subsequently submitted to a constant current reanodization, which results in the formation of nanoscopic channels through the barrier layer, reaching the aluminum surface (Figure S1C). Upon submitting the NAA layer to a final chemical etching step, the now weakened barrier layer dissolves at a faster rate than the pores' walls, leaving the bottom of the pores free of alumina.[57] Importantly enough, this final etching step, in addition to achieving the complete removal of the barrier layer, also leaves the bottom of the pores with nanoscopic longitudinal openings (Figure 2B). These openings play a crucial role in the infiltration of the layer in direct contact with the aluminum substrate as it allows the liquid to channel through the openings and allows overcoming the force exerted by the air being trapped at the bottom of the nanoscopic pores if they were sealed. The effect is seen visually, as when a drop of liquid is cast in the middle of the substrate, the liquid diffuses over the entire layer through capillarity. Therefore, the first layer of the assembly was readily infiltrated into the pores *via* spin-coating, in air, of a sol-gel precursor of titanium dioxide. Calcination of the substrates in a furnace at 500°C yielded the TiO_2 layer with no damage to the NAA porous structure nor to the aluminum substrate. Due to the thinness of the resulting nanostructured TiO_2 layer, obtaining a precise measurement of the layer thickness is complex using scanning electron microscopy (SEM), however, a rough estimate was possible using cross-section SEM images, as seen in Figure 2C. The image shows a TiO_2 layer with an approximate thickness of 40 nm.

The infiltration of the subsequent $MAPbI_3$ material into the NAA required careful optimization of the deposition conditions since, after the infiltration of the TiO_2 layer, the openings at the bottom of the pores are sealed to a significant extent, by the latter material. Our first attempts to drop-cast diluted solutions (0.25 and 0.5 mol L^{-1}) of $MAPbI_3$ precursors and placing the substrates on a hot plate, did not provide the expected homogeneous crystal growth originating from the bottom of the pores. Indeed, due to the highly crystalline nature of $MAPbI_3$, any sharp edge provides for a nucleation site that triggers the crystallization of $MAPbI_3$ from random locations on the NAA layer. We, therefore, turned our focus to spin-coating to achieve a more homogeneous filling of the pores. To facilitate the displacement of the air trapped at the bottom of the pores upon casting the solution of precursors, the substrates were placed under vacuum for a minute before being spun (see Supporting Information for details). A preliminary result of spin-coated-filled NAA in which a high concentration of precursors was used is depicted in Figure 3A,B. Similar to the results obtained from drop-casting (vide supra), one can observe from the SEM images, that large crystals have formed from random nucleation sites on the surface of the NAA layer. This effect seemed to be predominant regardless of the spinning velocity, implying that $MAPbI_3$ material is pulled out of the pores during the crystallization process, presumably by diffusion from a semiliquid state during the growth step. This is clearly evidenced from the voids (dark areas in Figure 3A,B) left after the film was dried.

The optimization of the precursors' concentration was, therefore, carried out, and the best results were obtained with a 2 mol L^{-1} concentration of PbI_2 and $MeNH_3I$. Lower concentrations of precursors led to partially filled pores and the formation of lumps on the surface of the NAA, an effect clearly seen on the image from Figure 3C,D.

Contrary to the 2.5 and 1.5 mol L^{-1} solutions, the 2 mol L^{-1} concentration showed to yield $MAPbI_3$-infiltrated layers with no lumps nor large crystalline aggregates on top of the NAA, as well as providing a high degree of pore-filling. The top views in Figure 3E,F show only a few areas with unfilled pores, while cross-section images recorded with a backscattered electrons detector (Figure 3G,H) confirm that the pores are on average filled to about half of their height. These images show how the filling is homogeneous across large areas of the substrate and can be extrapolated to the whole NAA layer. Noteworthy, the vast majority of the pores are filled from the bottom-up, with no significant voids at the bottom of the pores as observed in the layers manufactured from 1.5 and 2.5 mol L^{-1} solutions (see Figure S2). The spinning velocity was carefully optimized to provide for layers of an approximate 500 nm thickness; however, spinning speeds could only be varied within a very limited range without significantly impacting the homogeneity of the filling.

Additional to the SEM images, the NAA layers were further characterized using X-Ray diffraction using both Bragg-Brentano geometry and grazing incidence angles with an area detector. The conventional diffractograms clearly show that the $MAPbI_3$ layer is crystalline, and the crystals are from the typical tetragonal structure from the I4-cm space group, as expected for this combination of lead and iodine precursors.[58,59] A comparison with a layer deposited in identical conditions of concentration

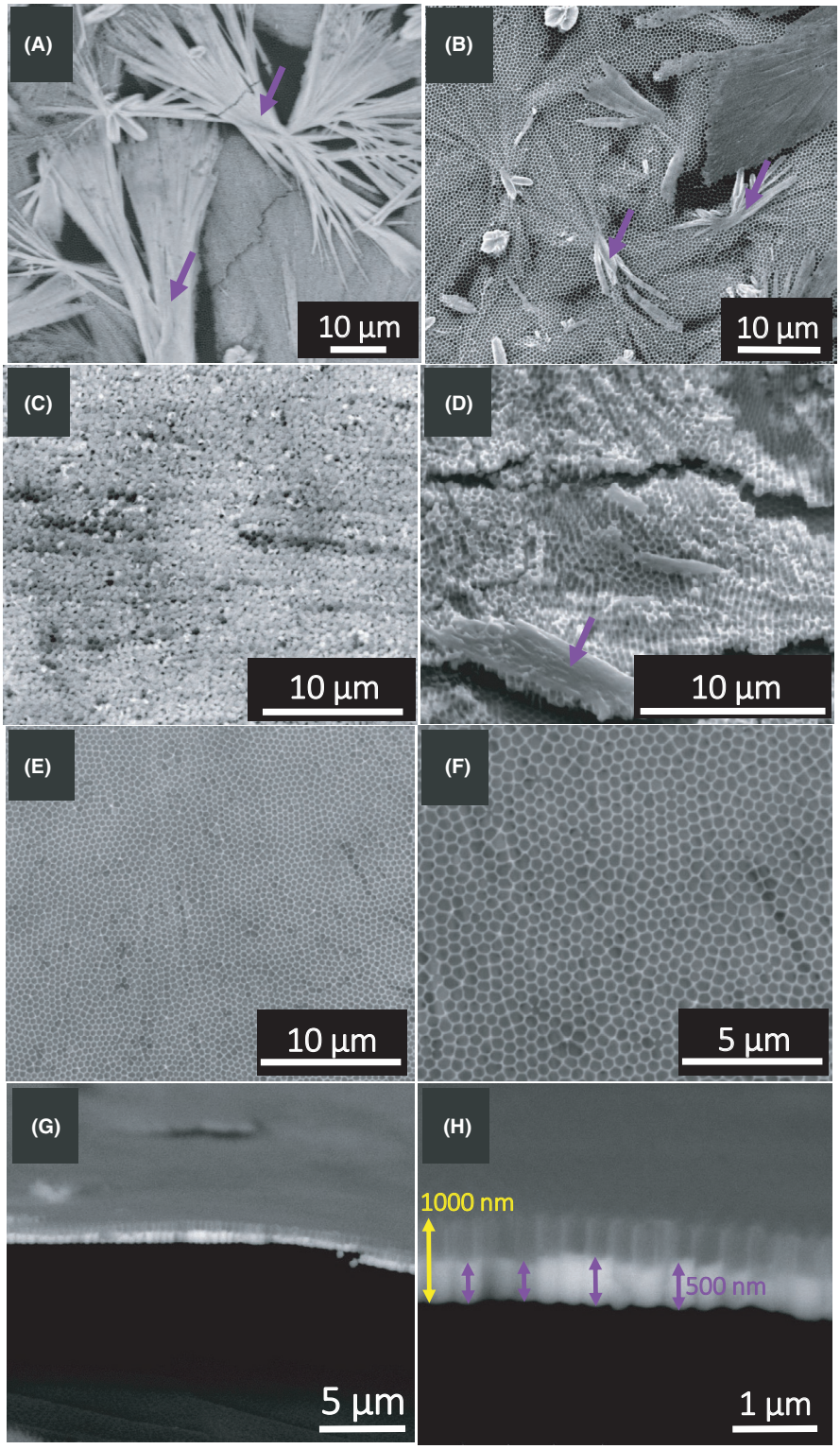

FIGURE 3 SEM images of NAA substrate filled with $MAPbI_3$ via spin-coating using a precursors concentration of 2.5 mol L^{-1} (A, B), 1.5 mol L^{-1} (C, D), and 2.0 mol L^{-1} (E, F). The $MAPbI_3$ layer is shown by the purple arrows. Pictures (G, H) are cross-section SEM images of the layers depicted in pictures (E, F) recorded with a backscattered electrons detector, where the brightness is proportional to the presence of higher atomic number elements. The $MAPbI_3$ layer is shown by the purple arrows while the yellow arrows show the pores' height. The scales are indicated in each picture

(2 mol L^{-1}) and spinning velocity on a bare aluminum substrate reveals that the crystallinity of the $MAPbI_3$ layer is somewhat similar in terms of crystallite size and volume, however, and quite importantly, the $MAPbI_3$ precursor solution has very poor film-forming properties on bare aluminum substrates, and the resulting films show extremely poor homogeneity up to the macroscopic level. A Pawley profile adjustment of the diffraction patterns allowed establishing that the $MAPbI_3$ crystallites are on average 208 nm large in the case of the NAA and 210 nm in the case of the bare aluminum (see Figure S3). These findings strongly support the evidence that the nucleation step is predominant in both cases, rather than the growth step, contrary to the NAA filled with 2.5 mol L-1 $MAPbI_3$ precursors where growth seems to be predominant. Due to the fact that the crystallites' size is similar in both NAA

and bare aluminum substrates, we concluded that the concentration of the $MAPbI_3$ precursors is determinant for the crystalline properties of the $MAPbI_3$ layer, rather than the confining effect of the pores. However, a comparison of the area images and diffractograms of both the perovskite deposited on bare aluminum substrates and on the NAA show some differences in texture.

That is, both the $MAPbI_3$ deposited on bare aluminum substrates and that infiltrated in the NAA pores show evidence of preferential crystalline orientation as seen by the mismatch between the peaks' intensity of the theoretical diffraction pattern and the experimental diffractograms (Figure 4A,D,E). In the case of the $MAPbI_3$ deposited on aluminum substrates, a correlation with the corresponding 2D diffractogram (area image in Figure 5A) confirms a preferential orientation as seen by the stronger intensity of the Debye rings in the out-of-plane direction for the 004/220-diffraction planes. The additional calculated 1D diffractograms with a preferential orientation toward the (004) or (220) planes show a fair match between the latter and the experiential diffractogram, advocating, therefore, that the crystallites are oriented with the 220-diffraction plane in the out-of-plane direction (Figure 4B-D).

A similar analysis applies to the $MAPbI_3$ layer infiltrated into the NAA. However, although 2D diffraction patterns in Figure 5B show a clear preferential orientation of the 220 or 004 planes in the out-of-plane direction, in this case, the 1D diffractogram (Figure 4E) does not allow to discriminate one preferential orientation with respect to the other since the intensity ratio of the corresponding diffraction peaks in not significantly changed compared to the calculated diffractogram of randomly oriented crystals (Figure 4A). It, therefore, results that the $MAPbI_3$ layer is composed of at least two groups of crystallites each having a preferential orientation. A closer look at the 2D diffractogram showed additionally a significant orientation toward the 202 plane, supposedly corresponding to a third group of crystallites with preferential orientation. To verify this hypothesis a calculated diffractogram corresponding to the sum of the diffractograms with a preferred orientation toward the 004, 220, and 202 planes was compared with the experimental diffractogram of the $MAPbI_3$ infiltrated in the NAA. Adjusting the ratio between the 3 fractions to 34%, 55%, and 11%, respectively, produced a fairly accurate correlation between the two sets of data (Figure 6).

To conclude, these results show that, presumably due to the fast kinetics of the nucleation and growth processes of the $MAPbI_3$, the NAA does not play a significant role as a scaffold for the homogeneous growth of large $MAPbI_3$ crystals within the cavities of the pores. However, the NAA has been shown to have a significant impact on the orientation of the crystallites with respect to the bare aluminum surface. This is in accordance with a previous study from Lee and coworkers where $MAPbI_3$ was shown to grow crystallites in the preferential <001> plane direction when infiltrated in NAA with up to 200 nm diameter.[39] The orientation is in our case less pronounced than in Lee and coworkers' work; however, it seems to follows their trend in which the orientation's magnitude decreases with the pore's diameter. Similarly, the orientation toward three different crystallographic planes may well be linked to the larger pore diameter of our NAA with respect to Lee's work. Despite these properties, the crystalline nature of the material fits with the prerequisites for a functional PSC device.

The next step is, therefore, the infiltration of the HTM, which was chosen to be spiro-OMeTAD for its widespread usage and effective hole transport properties even when thick layers are employed.[60] Indeed, in this particular

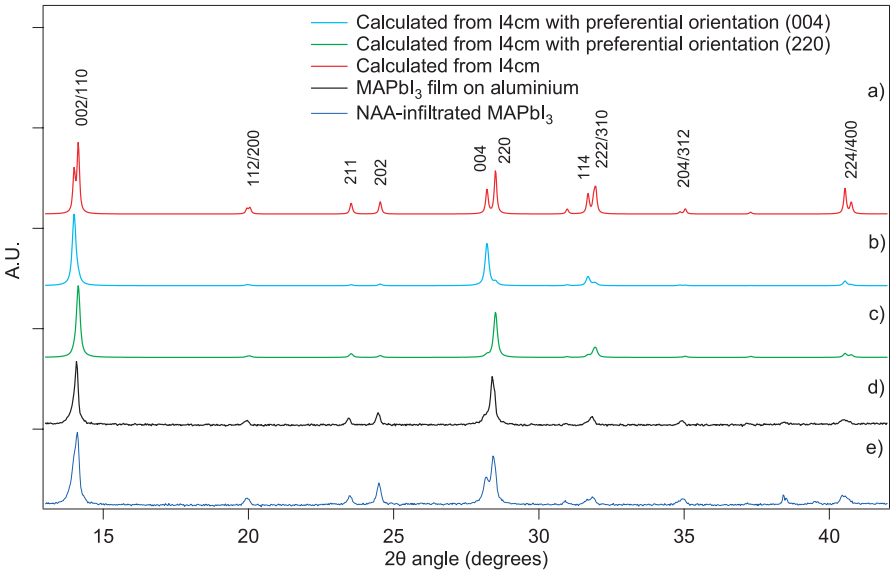

FIGURE 4 Calculated diffractograms of $MAPbI_3$ from the tetragonal structure (I4cm, a 8.849; b 8.849, c 12.642; at 293K) with no preferential orientation (red line), preferential orientation toward the (004) plane (blue line), preferential orientation toward the (220) plane (green line), and experimental diffractogram of the $MAPbI_3$ layer deposited on bare aluminum substrates (black line)

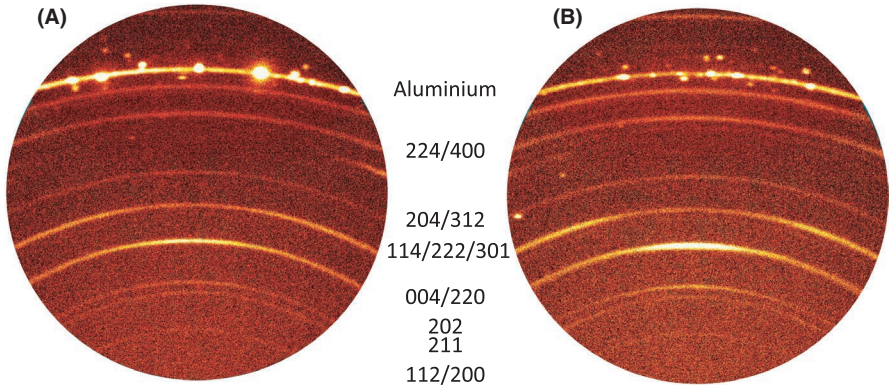

FIGURE 5 2D area images of grazing incidence XRD of the MAPBI3 layer deposited on bare aluminum substrates (A) and infiltrated in NAA layers (B). The Debye rings are indexed with the diffraction planes

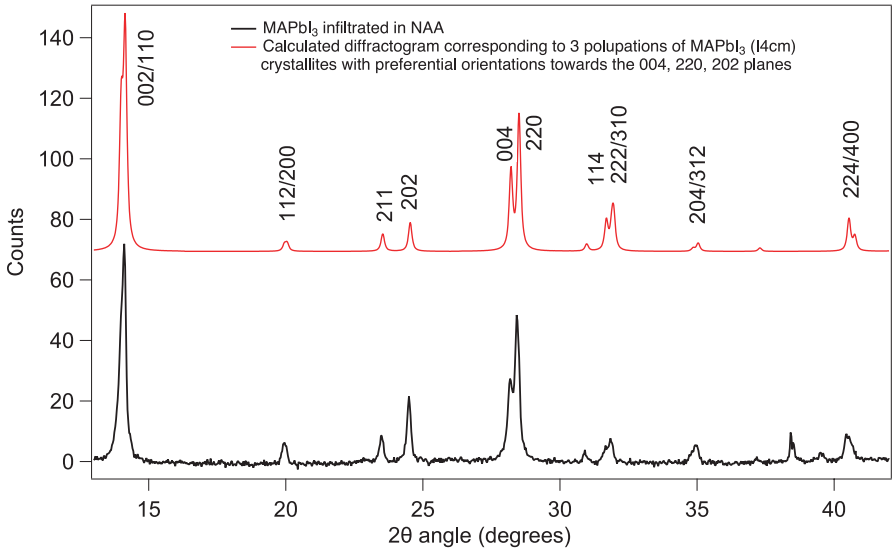

FIGURE 6 Sum of calculated diffractogram of $MAPbI_3$ from the tetragonal structure (I4cm, a 8.849; b 8.849, c 12.642; at 293K) with preferential orientation (preferential orientation toward the (004), (220), and (202) planes with 34%, 55%, and 11% respective contributions (red line), and experimental diffractogram of the $MAPbI_3$ layer deposited on NAA substrates (black line)

case, the spiro-OMeTAD layer was deposited to provide -additional to the hole conduction properties-for a complete leveling of the NAA pores top openings. This is a prerequisite for the subsequent deposition of the thin WO_3/Ag alternating layers composing the anode, to grant electrical continuity over the whole device surface. Therefore, the overall thickness of the spiro-OMeTAD layer resulted to be somewhat higher than optimum (ie >800 nm vs. 150 nm) and is expected to incur some resistive losses. However, these losses are a trade-off accounted for in our study, and are not expected to interfere with the operation of the device, since state-of-the-art PSC devices with up to 700 nm thick spiro-OMeTAD have been reported with high fill factors and efficiencies approaching 11%.[61]

The deposition of the spiro-OMeTAD layer was carried out *via* spin-coating as for the previous layers; however, it was found that the infiltration into the pores and the optimization of the layer thickness was less complex than in the case of the $MAPbI_3$. This is most probably due to the amorphous nature of the material, and to the fact that the pores were already partially filled with $MAPbI_3$ prior to the deposition of the HTM. Figure 7B,D show the effectiveness of spiro-OMeTAD in filling the pores and leveling the NAA layer before the cathode deposition. The impact of incomplete leveling is also shown, in Figure 7A-C, where the subsequently deposited anode forms bumps, whose shape follows the hexagonal pattern of the pores. This further highlights the importance of the HTM in leveling the surface of the NAA before the deposition of the anode. Consequently, when the spiro-OMeTAD is sufficiently thick the multilayer cathode displays a very flat surface over the area of the substrate with no obvious discontinuities, as seen in the SEM images (Figure 7E,F).

Figure 7G shows a cross-section SEM image (from a backscattered electrons detector) of a complete device where all the layers are stacked above one another. Each material is highlighted with a different color and the thicknesses of the $MAPbI_3$, spiro-OMeTAD, and semi-transparent electrode are estimated to be 500, 900, and 230 nm, respectively. The cathode shows to be completely homogeneous and without disruption, guarantying electrical conduction over the whole surface of the device.

Finally, the electrical properties of the full devices were characterized. The current-voltage *(J-V)* characteristics of the best performing PSCs devices measured in the dark and under simulated AM1.5G illumination are shown in Figure 8. The main properties of the devices are summarized in Table 1. All in all, the devices displayed

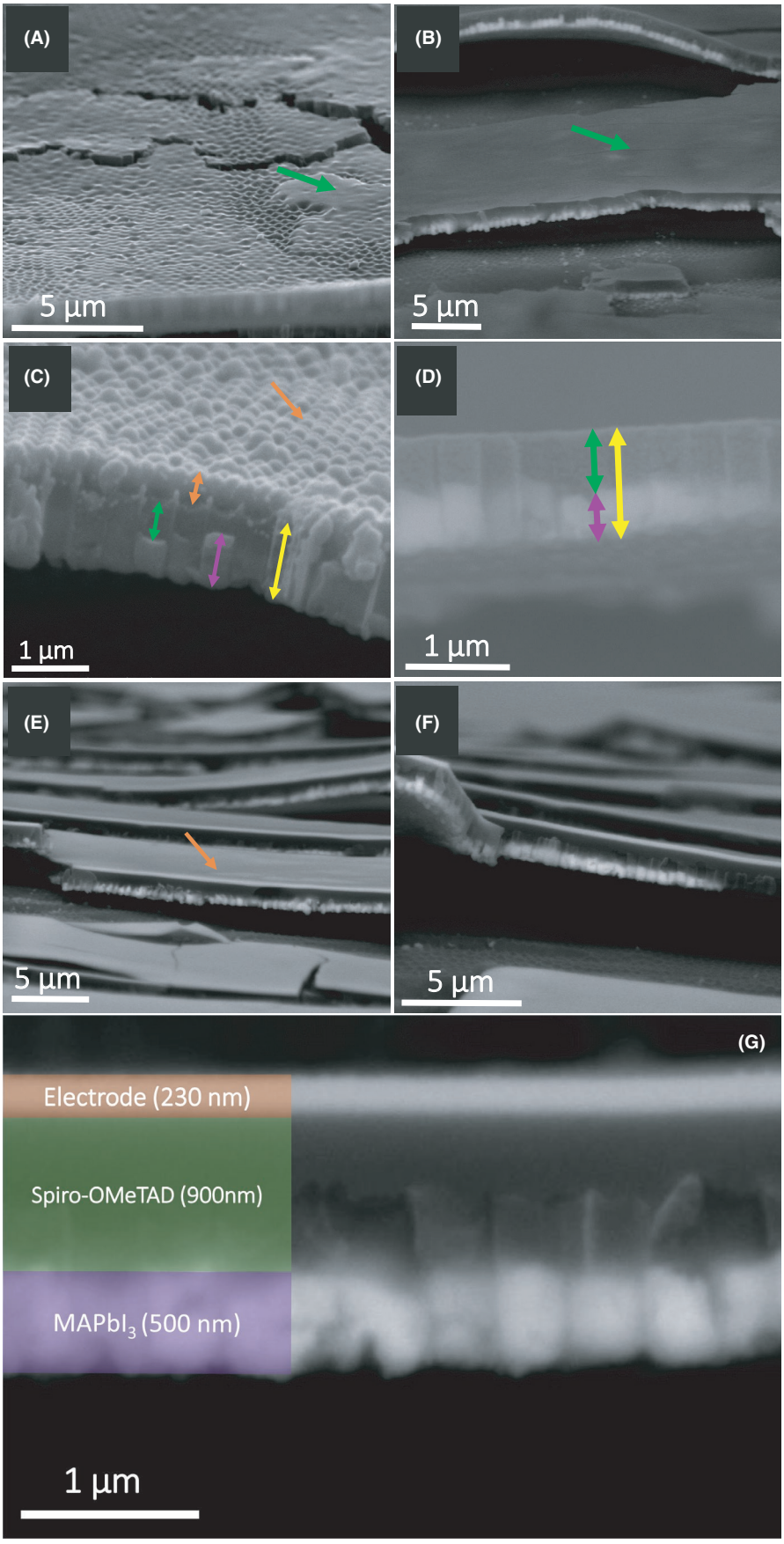

FIGURE 7 A, SEM image of NAA substrate filled with $MAPbI_3$ (via spin-coating using a precursors concentration of 2.0 mol L^{-1}) with inhomogeneous coverage with a spiro-OMeTAD layer. B, SEM image of NAA substrate filled with $MAPbI_3$ with homogeneous coverage with a spiro-OMeTAD layer (backscattered electrons detector). C, Cross-section SEM image of the afore-mentioned sample. D, SEM image of NAA substrate filled with $MAPbI_3$ with inhomogeneous coverage of spiro-OMeTAD and upper WO_3/Ag anode. E-G, SEM images of a complete NAA-PSC device. The $MAPbI_3$, spiro-OMeTAD and the semi-transparent electrode layers are marked by purple, green and orange arrows, respectively. The yellow double arrow denotes the pores thickness. The scales are indicated in each picture

modest values of open-circuit voltage (V_{OC}), short-circuit current density (J_{SC}), fill factor (FF), and power conversion efficiency (PCE) with respect to state-of-the-art PSC devices, however, and most importantly, the shape of the *J-V* characteristics provide unequivocal confirmation that an ohmic contact is established between the aluminum substrate and the successive layers. Indeed, the rectifying behavior demonstrates that electrons are injected into the aluminum cathode and that a built-in field is present under open-circuit conditions.

The less-than-optimum *J-V* characteristics are most probably due to a combination of factors linked to the morphological complexity of the device. First of all, the multilayer arrangement inside pores of such a small size, a premiere in this study, is likely responsible for the formation of voids, due to air being trapped between the layers during the deposition of the successive layers. This can be seen in Figure 7G. Similar voids would probably exist between the TiO_2 and $MAPbI_3$ layer, although not clearly characterized here. Second, the very thick layer of HTM, necessary to level the NAA layer, although not expected to compromise the function of the device to a large extent, is most probably responsible for significant losses. The high density of structural defects together with the thickness of the overall device are likely responsible for a great amount of charge trapping as well as fast rates of recombination dynamics with respect to charge percolation/sweep out to the respective electrodes.[62-65] Then, finally and quite importantly the very low photovoltaic effect can, to a very significant extent, be attributed to the strong absorbance of the anode. Indeed, a UV-Visible characterization of the pristine alternating WO_3/Ag layers showed that the layer possesses a stronger absorbance than that expected from the literature (see Supporting Information for details). Further optimization would be necessary to find a better trade-off between high conductivity and low absorbance.

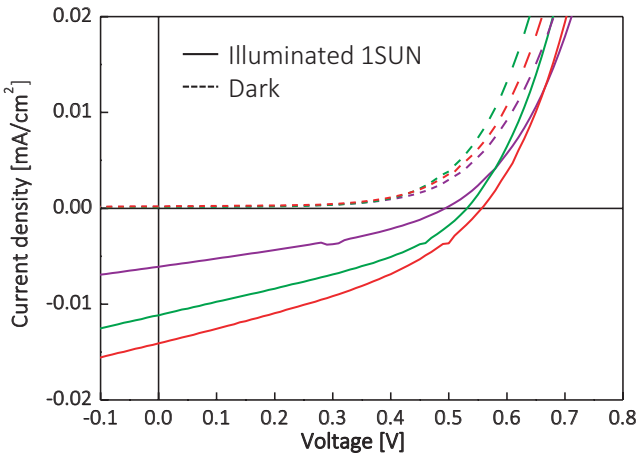

FIGURE 8 *J-V* characteristics of the best performing NAA-PSCs devices in the dark and under AM 1.5G irradiation

3 | CONCLUSION

This study is, to the best of our knowledge one of the first examples of devices in which NAA is used to contain the components of the device and the aluminum substrate is used as an electrode. We demonstrated that an ohmic contact can be established between the latter substrate and the material the NAA is filled with. Moreover, the application of the concept to PV devices of such complexity as PSC clearly demonstrate the applicability of NAA for the fabrication of advanced electronic devices, such as batteries, sensors, photovoltaics, or light-emitting devices in which the confinement properties of the NAA can be put to use to shape the materials at the nanoscopic level and where the aluminum substrate can be used directly as an electrical contact. Interestingly enough, and contrary to our expectations, only a subtle difference in the crystallization behavior of the $MAPbI_3$ was observed when confined in nanosized pores with respect to when the $MAPbI_3$ is deposited on a flat surface. This effect is likely linked to the very fast crystal growth kinetics of the $MAPbI_3$ with respect to the nucleation step. This is further confirmed by the fact that the presence of numerous nucleation sites resulting from the highly porous nature of the NAA does not have a significant impact on the size and crystalline volume of the infiltrated $MAPbI_3$ material with respect to a $MAPbI_3$ layer deposited on bare aluminum substrates. Future work is currently underway to gain a deeper understanding of the latter experimental findings. As such, infiltrations of $MAPbI_3$ precursors with different PbI_2/$MeNH_3I$ ratios are currently been investigated as it has been shown that the formation of crystalline $MAPbI_3$ follows different paths depending on the latter ratio.[66] Additionally, future work will include reducing the thickness of the NAA layer, reducing the thickness of the HTM layer, and decreasing the absorption of the semi-transparent anode. Although the manufacture of PSC devices using such type of NAA scaffold has revealed challenging, this study holds great promise for future applications. Indeed, the versatile nature of the NAA pores, which can be etched selectively using mild acidic solutions at low temperature, makes it a very good candidate to fabricate electrodes with textured materials. Indeed, after the pores have been filled with a water-resistant material one could simply etch entirely or partially the walls of the container's pores to reveal a nearly perfect arrangement of pillars connected ohmically to the aluminum substrate with a very high surface area. This concept is not limited to the pore size described in this article and can be applied to pore sizes ranging from 10 nm to over 500 nm in diameter.

TABLE 1 NAA-PCSs devices properties at 1SUN (AM 1.5G) illumination

	V_{oc}[a] [V]	J_{sc}[b] [mAcm^{-2}]	FF[c] [%]	PCE[d] [%]
Purple	0.49	0.006	38	0.011
Green	0.53	0.011	36	0.021
Red	0.56	0.014	36	0.028

[a]Open-circuit voltage.
[b]Short circuit current density.
[c]Fill factor.
[d]Power conversion efficiency.

4 | EXPERIMENTAL SECTION/METHODS

4.1 | Titanium dioxide infiltration

First, a titanium dioxide sol-gel precursor solution (TiO_x-solution) was prepared in an N_2-filled glovebox, *via* the sol-gel method by mixing 0.2 ml of titanium (IV) isopropoxide ($Ti[OCH(CH_3)_2]_4$) with 0.1 mL of 2-methoxy ethanol ($CH_3OCH_2CH_2OH$) and 1 mL of ethanolamine ($H_2NCH_2CH_2OH$).[67,68] Subsequently, the TiO_x-solution was diluted in anhydrous methanol (CH_3OH) with a volume ratio of 1:3 (TiO_x-precursor solution: CH_3OH).[69] Secondly, 100 μL of the diluted TiO_x-solution were deposited on the top of different barrier layer-free NAA (f-NAA) substrates. The solution was left standing on top of the substrates for 30s, to let the solution diffuse through the pores, and the substrates were spun at 4000 rpm (2160 rpm s^{-1}) for 90 seconds. The substrates were subsequently left in air at room temperature for 1 hour, heated at 150ºC for 10 minutes, and finally heated at 500ºC for 30 minutes in a furnace.

4.2 | Methylammonium lead iodide perovskite infiltration

Several $MAPbI_3$ perovskite precursor solutions with different concentrations (1.5, 2.0, 2.5 mol L^{-1}) were prepared in an N_2-filled glovebox from lead iodide (PbI_2) and methylammonium iodide ($MeNH_3I$, MAI) using anhydrous *N*,*N*-dimethylformamide (DMF) as solvent. Each precursor was dissolved in 500 μL of DMF separately. To promote the dissolution of the lead salt, PbI_2 was heated in DMF at 150ºC for 10 minutes on a hot plate and left to cool down to room temperature after which MAI was added. The precursor solution was subsequently deposited on the NAA substrate as follows: 100 μL of $MAPbI_3$ perovskite precursor solution was cast on top of different f-NAA-TiO_2 substrates. To facilitate the displacement of the air trapped at the bottom of the nanopores, the substrates were placed under vacuum for a minute before being spun. To do so, a funnel connected to a vacuum pump was tightly fitted to the spin coater chuck using a silicone rubber seal after the precursor solution was cast on top of the substrate. The substrates were spin-coated at 4000 rpm (3996 rpm s^{-1}) for 45 seconds, to obtain the desired nanostructured $MAPbI_3$ perovskite layer with a thickness ranging from 400 nm and 600 nm. Finally, the substrates were placed in a hotplate and were annealed at 100°C for 1 hour to obtain crystalline $MAPbI_3$ perovskite films.

4.3 | 2,2′,7,7′-Tetrakis[N,N-di(4-methoxyphenyl)amino]-9,9′spirobifluorene infiltration

Solutions of 2,2′,7,7′-Tetrakis[*N*,*N*-di(4-methoxyphenyl)amino]-9,9′spirobifluorene (spiro-OMeTAD) with different concentrations were prepared, in an N_2-filled glovebox, by dissolving different amounts of spiro-OMeTAD in 1 mL of anhydrous chlorobenzene. Secondly, 100 μL of each solution was deposited on the top of several f-NAA-TiO_2-$MAPbI_3$ substrates. The spiro-OMeTAD layer thickness was adjusted *via* adjusting the concentration of the solution and spin-coating speed. A 72 mg mL^{-1} spiro-OMeTAD solution was spin-coated at two different spin speeds (Ss): $Ss_1 = 1000$ rpm and $Ss_2 = 1500$ rpm. After these tests, the spiro-OMeTAD layer infiltration was optimized by testing two more spiro-OMeTAD solution concentrations (C): $C_1 = 105$ mg mL^{-1} and $C_2 = 140$ mg mL^{-1}, using the same spinning conditions in its deposition.

4.4 | Deposition of the anode

After the spiro-OMeTAD had been deposited, the substrates were placed in a thermal evaporator chamber (vacuum pressure $<3 \times 10^{-6}$ mbars, in an N_2-filled glovebox), and the semi-transparent electrode was deposited using a shadow mask to pattern the electrode as described by Jun Hee Han et al[70] Tungsten trioxide (WO_3) and silver (Ag) were evaporated successively from a tungsten boat at a constant rate (1-2 A/s).[71] The final anode had the following structure: WO_3 (50 nm)/Ag (12 nm)/WO_3 (105 nm)/Ag (12 nm)/WO_3 (50 nm).

The transmittance spectra in the UV-Visible wavelength range (300-800 nm) of the semi-transparent anode and the reference glass substrate is shown in Figure S4.

ACKNOWLEDGMENTS

This work was supported by the Spanish Ministerio de Ciencia, Innovación y Universidades (MICINN/FEDER) RTI2018-094040-B-I00 and by the Agency for Management of University and Research Grants (AGAUR) ref. 2017-SGR-1527.

CONFLICT OF INTEREST

The authors declare that there is no conflict of interest.

ORCID

María P. Montero-Rama https://orcid.org/0000-0002-4430-8723
Aurelien Viterisi https://orcid.org/0000-0002-9967-9484
Josep Ferré-Borrull https://orcid.org/0000-0002-5210-5133
Lluis F. Marsal https://orcid.org/0000-0002-5976-1408

REFERENCES

1. Masuda H, Fukuda K. Ordered metal nanohole arrays made by a two-step replication of honeycomb structures of anodic alumina. *Science*. 1995;268(5216):1466-1468.
2. Masuda H, Yamada H, Satoh M, Asoh H, Nakao M, Tamamura T. Highly ordered nanochannel-array architecture in anodic alumina. *Appl Phys Lett*. 1997;71(19):2770-2772.
3. Masuda H, Yada K, Osaka A. Self-ordering of cell configuration of anodic porous alumina with large-size pores in phosphoric acid solution. *Jpn J Appl Phys*. 1998;37(Part 2(11A):L1340-L1342.
4. Ferré-Borrull J, Xifré-Pérez E, Pallarès J, Marsal LF. Optical properties of nanoporous anodic alumina and derived applications. In: *Nanoporous Alumina*, Vol. 219. Springer International Publishing; 2015:185-217.
5. Stępniowski WJ, Bojar Z. Nanoporous anodic aluminum oxide: fabrication, characterization, and applications. In: Aliofkhazraei M, Makhlouf ASH, eds. *Handbook of Nanoelectrochemistry*. Springer International Publishing; 2016:593-645.
6. Mijangos C, Hernández R, Martín J. A review on the progress of polymer nanostructures with modulated morphologies and properties, using nanoporous AAO templates. *Prog Polym Sci*. 2016;54-55:148-182.
7. Ruiz-Clavijo A, Caballero-Calero O, Martín-González M. Revisiting anodic alumina templates: from fabrication to applications. *Nanoscale*. 2021;13(4):2227-2265.
8. Zhou Z, Nonnenmann SS. Progress in nanoporous templates: beyond anodic aluminum oxide and towards functional complex materials. *Materials*. 2019;12(16):2535.
9. Md Jani AM, Losic D, Voelcker NH. Nanoporous anodic aluminium oxide: advances in surface engineering and emerging applications. *Prog Mater Sci*. 2013;58(5):636-704.
10. Ferré-Borrull J, Rahman MM, Pallarès J, Marsal LF. Tuning nanoporous anodic alumina distributed-Bragg reflectors with the number of anodization cycles and the anodization temperature. *Nanoscale Res Lett*. 2014;9(1):416.
11. Foong TRB, Liang YN, Hu X. Anodic aluminum oxide (AAO) templates on transparent conducting glass (TCO) coated glass: new prospects for a mature nano-fabrication tool. *Nanosci Nanotechnol Lett*. 2012;4(5):494-504.
12. Santos A, Kumeria T, Losic D. Nanoporous anodic alumina: a versatile platform for optical biosensors. *Materials*. 2014;7(6):4297-4320.
13. Law CS, Lim SY, Abell AD, Voelcker NH, Santos A. Nanoporous anodic alumina photonic crystals for optical chemo- and biosensing: fundamentals, advances, and perspectives. *Nanomaterials*. 2018;8(10):788.
14. Amouzadeh Tabrizi M, Ferre-Borrull J, Marsal LF. Advances in optical biosensors and sensors using nanoporous anodic alumina. *Sensors*. 2020;20(18):5068.
15. Ferré-Borrull J, Pallarès J, Macías G, Marsal LF. Nanostructural engineering of nanoporous anodic alumina for biosensing applications. *Materials*. 2014;7(7):5225-5253.
16. Pol L, Acosta LK, Ferré-Borrull J, Marsal LF. Aptamer-based nanoporous anodic alumina interferometric biosensor for real-time thrombin detection. *Sensors*. 2019;19(20):4543.
17. Sousa CT, Leitao DC, Proenca MP, Ventura J, Pereira AM, Araujo JP. Nanoporous alumina as templates for multifunctional applications. *Appl Phys Rev*. 2014;1(3):031102.
18. Jeon G, Yang SY, Kim JK. Functional nanoporous membranes for drug delivery. *J Mater Chem*. 2012;22(30):14814.
19. Gultepe E, Nagesha D, Sridhar S, Amiji M. Nanoporous inorganic membranes or coatings for sustained drug delivery in implantable devices. *Adv Drug Deliv Rev*. 2010;62(3):305-315.
20. Kapruwan P, Ferré-Borrull J, Marsal LF. Nanoporous anodic alumina platforms for drug delivery applications: recent advances and perspective. *Adv Mater Interfaces*. 2020;7(22):2001133.
21. Jiang Q, Ward MD. Crystallization under nanoscale confinement. *Chem Soc Rev*. 2014;43(7):2066-2079.
22. Fan Z, Razavi H, Do J, et al. Three-dimensional nanopillar-array photovoltaics on low-cost and flexible substrates. *Nature Mater*. 2009;8(8):648-653.
23. Choi K, Yoon Y, Jung J, et al. Super-antireflective structure films with precisely controlled refractive index profile. *Adv Opt Mater*. 2017;5(3):1600616.
24. Wen L, Xu R, Mi Y, Lei Y. Multiple nanostructures based on anodized aluminium oxide templates. *Nature Nanotech*. 2017;12(3):244-250.
25. Balderrama VS, Albero J, Granero P, et al. Design, fabrication and charge recombination analysis of an interdigitated heterojunction nanomorphology in P3HT/PC 70 BM solar cells. *Nanoscale*. 2015;7(33):13848-13859.
26. Kang G, Bae K, Nam M, Ko D-H, Kim K, Padilla WJ. Broadband and ultrahigh optical haze thin films with self-aggregated alumina nanowire bundles for photovoltaic applications. *Energy Environ Sci*. 2015;8(9):2650-2656.
27. Wu Y, Assaud L, Kryschi C, et al. Antimony sulfide as a light absorber in highly ordered, coaxial nanocylindrical arrays: preparation and integration into a photovoltaic device. *J Mater Chem A*. 2015;3(11):5971-5981.
28. Kwon H-C, Kim A, Lee H, Lee D, Jeong S, Moon J. Parallelized nanopillar perovskites for semitransparent solar cells using an anodized aluminum oxide scaffold. *Adv Energy Mater*. 2016;6(20):1601055.
29. Santos A, Vojkuvka L, Pallarés J, Ferré-Borrull J, Marsal LF. In situ electrochemical dissolution of the oxide barrier layer of porous anodic alumina fabricated by hard anodization. *J Electroanal Chem*. 2009;632(1–2):139-142.

30. Jagminas A, Kurtinaitienė M, Angelucci R, Valinčius G. Modification of alumina barrier-layer through re-anodization in an oxalic acid solution with fluoride additives. *Appl Surf Sci*. 2006;252(6):2360-2367.
31. Shaban M, Hamdy H, Shahin F, Park J, Ryu S-W. Uniform and reproducible barrier layer removal of porous anodic alumina membrane. *J Nanosci Nanotech*. 2010;10(5):3380-3384.
32. Sulka GD, Moshchalkov V, Borghs G, Celis J-P. Electrochemical impedance spectroscopic study of barrier layer thinning in nanostructured aluminium. *J Appl Electrochem*. 2007;37(7):789-797.
33. Zhao X, Seo S-K, Lee U-J, Lee K-H. Controlled electrochemical dissolution of anodic aluminum oxide for preparation of open-through pore structures. *J Electrochem Soc*. 2007;154(10):C553.
34. Nielsch K, Müller F, Li A-P, Gösele U. Uniform nickel deposition into ordered alumina pores by pulsed electrodeposition. *Adv Mater*. 2000;12(8):582-586.
35. Montero-Rama MP, Viterisi A, Eckstein C, Ferré-Borrull J, Marsal LF. In-situ removal of thick barrier layer in nanoporous anodic alumina by constant current Re-anodization. *Surf Coat Technol*. 2019;380:125039.
36. Demchyshyn S, Roemer JM, Groiß H, et al. Confining metal-halide perovskites in nanoporous thin films. *Sci Adv*. 2017;3(8):e1700738.
37. Zhang Z, Wang M, Ren L, Jin K. (2017) Tunability of band gap and photoluminescence in $CH_3NH_3PbI_3$ films by anodized aluminum oxide templates. *Sci Rep*. 1918;7(1). https://doi.org/10.1038/s41598-017-02144-x
38. Waleed A, Tavakoli MM, Gu L, et al. All inorganic cesium lead iodide perovskite nanowires with stabilized cubic phase at room temperature and nanowire array-based photodetectors. *Nano Lett*. 2017;17(8):4951-4957.
39. Lee S, Feldman J, Lee SS. Nanoconfined crystallization of $MAPbI_3$ to probe crystal evolution and stability. *Cryst Growth Des*. 2016;16(8):4744-4751.
40. Seo SW, Jeon J-O, Seo JW, et al. Compositional and interfacial modification of $Cu_2ZnSn(S,Se)_4$ thin-film solar cells prepared by electrochemical deposition. *Chemsuschem*. 2016;9(5):439-444.
41. Berhe TA, Su W-N, Chen C-H, et al. Organometal halide perovskite solar cells: degradation and stability. *Energy Environ Sci*. 2016;9(2):323-356.
42. Lin M-C, Nandan B, Chen H-L. Mediating polymer crystal orientation using nanotemplates from block copolymer microdomains and anodic aluminium oxide nanochannels. *Soft Matter*. 2012;8(28):7306.
43. Safari M, Leon Boigues L, Shi G, et al. Effect of nanoconfinement on the isodimorphic crystallization of poly(butylene succinate-*ran*-caprolactone) random copolymers. *Macromolecules*. 2020;53(15):6486-6497.
44. Wu H, Higaki Y, Takahara A. Molecular self-assembly of one-dimensional polymer nanostructures in nanopores of anodic alumina oxide templates. *Prog Polym Sci*. 2018;77:95-117.
45. Hamilton BD, Weissbuch I, Lahav M, Hillmyer MA, Ward MD. Manipulating crystal orientation in nanoscale cylindrical pores by stereochemical inhibition. *J Am Chem Soc*. 2009;131(7):2588-2596.
46. Su C, Chen Y, Shi G, et al. Crystallization kinetics of poly(ethylene oxide) under confinement in nanoporous alumina studied by in situ X-ray scattering and simulation. *Langmuir*. 2019;35(36):11799-11808.
47. Jeong W, Kye M, Han S, Choi JS, Lim Y. Inhibition of multimolecular RNA–protein interactions using multitarget-directed nanohybrid system. *ACS Appl Mater Interfaces*. 2017;9(13):11537-11545.
48. Meng L, You J, Guo T-F, Yang Y. Recent advances in the inverted planar structure of perovskite solar cells. *Acc Chem Res*. 2016;49(1):155-165.
49. Green MA, Ho-Baillie A, Snaith HJ. The emergence of perovskite solar cells. *Nature Photon*. 2014;8(7):506-514.
50. Jung JH, Kim S, Kim H, Park J, Oh JH. High-performance flexible organic nano-floating gate memory devices functionalized with cobalt ferrite nanoparticles. *Small*. 2015;11(37):4976-4984.
51. Gao P, Grätzel M, Nazeeruddin MK. Organohalide lead perovskites for photovoltaic applications. *Energy Environ Sci*. 2014;7(8):2448-2463.
52. Manser JS, Saidaminov MI, Christians JA, Bakr OM, Kamat PV. Making and breaking of lead halide perovskites. *Acc Chem Res*. 2016;49(2):330-338.
53. Grancini G, Sai Santosh Kumar R, Maiuri M, et al. Panchromatic "dye-doped" polymer solar cells: from femtosecond energy relays to enhanced photo-response. *J Phys Chem Lett*. 2013;4(3):442-447.
54. Lee MM, Teuscher J, Miyasaka T, Murakami TN, Snaith HJ. Efficient hybrid solar cells based on meso-superstructured organometal halide perovskites. *Science*. 2012;338(6107):643-647.
55. Stranks SD, Eperon GE, Grancini G, et al. Electron-hole diffusion lengths exceeding 1 micrometer in an organometal trihalide perovskite absorber. *Science*. 2013;342(6156):341-344.
56. Wehrenfennig C, Eperon GE, Johnston MB, Snaith HJ, Herz LM. High charge carrier mobilities and lifetimes in organolead trihalide perovskites. *Adv Mater*. 2014;26(10):1584-1589.
57. Despite being commonly refered to as alumina, the oxide forming upon aluminium anodization is in reality mostly composed of amorphous aluminium hydroxide oxide (AlOOH) with varying amounts of impurities (phosphate ions). This is the reason why, as opposed to pure Al_2O_3, dilute solutions of weak acids dissolve it readily.
58. Baikie T, Fang Y, Kadro JM, et al. Synthesis and crystal chemistry of the hybrid perovskite (CH3NH3)PbI3 for solid-state sensitised solar cell applications. *J Mater Chem A*. 2013;1(18):5628.
59. Oku T. Crystal structures of CH3NH3PbI3 and related perovskite compounds used for solar cells. In: Kosyachenko LA, ed. *Solar Cells – New Approaches and Reviews*. InTech; 2015. https://doi.org/10.5772/59284
60. Calió L, Kazim S, Grätzel M, Ahmad S. Hole-transport materials for perovskite solar cells. *Angew Chem Int Ed*. 2016;55(47):14522-14545.
61. Kim G-W, Shinde DV, Park T. Thickness of the hole transport layer in perovskite solar cells: performance versus reproducibility. *RSC Adv*. 2015;5(120):99356-99360.
62. O'Regan BC, Barnes PRF, Li X, Law C, Palomares E, Marin-Beloqui JM. Optoelectronic studies of methylammonium lead iodide perovskite solar cells with mesoporous TiO_2: separation of electronic and chemical charge storage, understanding two recombination lifetimes, and the evolution of band offsets during J–V hysteresis. *J Am Chem Soc*. 2015;137(15):5087-5099.
63. Johnston MB, Herz LM. Hybrid perovskites for photovoltaics: charge-carrier recombination, diffusion, and radiative efficiencies. *Acc Chem Res*. 2016;49(1):146-154.

64. Lopez-Varo P, Jiménez-Tejada JA, García-Rosell M, et al. Device physics of hybrid perovskite solar cells: theory and experiment. *Adv Energy Mater*. 2018;8(14):1702772.
65. Chen J, Park N. Causes and solutions of recombination in perovskite solar cells. *Adv Mater*. 2019;31(47):1803019.
66. Moore DT, Sai H, Tan KW, et al. Crystallization kinetics of organic-inorganic trihalide perovskites and the role of the lead anion in crystal growth. *J Am Chem Soc*. 2015;137(6):2350-2358.
67. Kim JY, Kim SH, Lee H-H, et al. New architecture for high-efficiency polymer photovoltaic cells using solution-based titanium oxide as an optical spacer. *Adv Mater*. 2006;18(5):572-576.
68. Sánchez JG, Balderrama VS, Garduño SI, et al. Impact of inkjet printed ZnO electron transport layer on the characteristics of polymer solar cells. *RSC Adv*. 2018;8(24):13094-13102.
69. Sánchez JG, Balderrama VS, Estrada M, et al. Stability study of high efficiency polymer solar cells using TiOx as electron transport layer. *Sol Energy*. 2017;150:147-155.
70. Han JH, Kim D, Jeong EG, et al. Highly conductive transparent and flexible electrodes including double-stacked thin metal films for transparent flexible electronics. *ACS Appl Mater Interfaces*. 2017;9(19):16343-16350.
71. Cambarau W, Viterisi A, Ryan JW, Palomares E. Small molecule-based tandem solar cells with solution-processed and vacuum-processed photoactive layers. *Chem Commun*. 2014;50(40):5349-5351.

SUPPORTING INFORMATION

Additional supporting information may be found in the online version of the article at the publisher's website.

How to cite this article: Montero-Rama MP, Viterisi A, Ferré-Borrull J, Marsal LF. Nanoporous anodic alumina with ohmic contact between substrate and infill: Application to perovskite solar cells. *Energy Sci Eng*. 2022;10:30–42. https://doi.org/10.1002/ese3.1002